Article

Narrow electroluminescence linewidths for reduced nonradiative recombination in organic solar cells and near-infrared light-emitting diodes

Quan Liu, Sander Smeets, Sigurd Mertens, ..., Jan D'Haen, Wouter Maes, Koen Vandewal

quan.liu@uhasselt.be (Q.L.)
koen.vandewal@uhasselt.be (K.V.)

Highlights

Nonradiative decay limits the performance of organic optoelectronics

Emission linewidth correlates with nonradiative losses

Low-molecular-weight PM6:Y16F has nonradiative voltage losses as low as 155 mV

Optimized PM6:Y16F blend has an EQE_{EL} among the best fluorescent NIR-OLEDs

Article

Narrow electroluminescence linewidths for reduced nonradiative recombination in organic solar cells and near-infrared light-emitting diodes

Quan Liu,[1,2,*] Sander Smeets,[1,2] Sigurd Mertens,[1,2] Yuxin Xia,[1,2] Andrea Valencia,[1,2] Jan D'Haen,[1,2] Wouter Maes,[1,2] and Koen Vandewal[1,2,3,*]

SUMMARY

The minimization of nonradiative recombination losses is essential to transcend the efficiency of state-of-the-art organic solar cells (OSCs) and near-infrared (NIR) organic light-emitting diodes (OLEDs). Indeed, reduced nonradiative processes will result in high electroluminescence (EL), external quantum efficiency (EQE$_{EL}$), and low nonradiative voltage losses ($\Delta V_{OC,nr}$) for OSCs. Here, we study the EL properties of a set of polymer-small molecule blends and find a relationship between the EL emission linewidth, EQE$_{EL}$, and $\Delta V_{OC,nr}$. Based on these findings, we reduce $\Delta V_{OC,nr}$ from the typical values around 250 mV down to an unprecedented value of 155 mV using a blend comprising a low-molecular-weight PM6 polymer donor and a highly emissive nonfullerene acceptor (Y16F). Importantly, the PM6:Y16F blend yields an EQE$_{EL}$ (0.52%) among the best reported fluorescent NIR-OLEDs in the 900-nm range. These findings clearly indicate the existence of organic material blends that combine both excellent photovoltaic and electroluminescent properties.

INTRODUCTION

The performance of current organic optoelectronic devices, especially in the near-infrared (NIR) region, is limited by strong nonradiative transition pathways governed by the so-called "energy-gap law."[1] This severely restricts the number of emitters suitable for NIR organic light-emitting diodes (NIR-OLEDs), while for NIR-harvesting organic solar cells (OSCs), it results in higher nonradiative open-circuit voltage losses ($\Delta V_{OC,nr}$) as compared with those of inorganic or perovskite-based technologies and thus lower power-conversion efficiencies (PCEs). Voltage losses in OSCs are linked to the external quantum efficiency of electroluminescence (EQE$_{EL}$), measured when a forward bias is applied to the device.[2,3]

$$\Delta V_{OC,nr} \approx -\frac{k_B T}{q} \ln(EQE_{EL}) \qquad \text{(Equation 1)}$$

In order to bring the open-circuit voltage (V_{OC}) closer to the optical gap, the energy offset between either the highest occupied or lowest unoccupied molecular orbital (HOMO or LUMO, respectively) energy levels of the donor (D) or acceptor (A) molecules needs to be minimized, and the lower gap material in the blend should be highly emissive.[4] Following these design rules, recent newly emerging donor-nonfullerene acceptor (NFA) blends with low-energy-offset yield high-efficiency OSCs (over 15%) with EQE$_{EL}$ values in the 0.001%–0.05% range, leading to $\Delta V_{OC,nr}$ on the order of 0.2–0.3 V.[5–15] The low-gap component of these devices is the NFA

Context & scale

Organic solar cells (OSCs) using nonfullerene acceptors have been steadily improving over the past few years, and their single-junction power-conversion efficiency now surpasses 18%. While promising, the currently best devices still suffer from relatively large nonradiative recombination voltage losses ($\Delta V_{OC, nr}$) as compared with inorganic or perovskite solar cells, typically around 250 mV. Further enhancement of the efficiency to values over 20% requires a reduction of $\Delta V_{OC, nr}$, corresponding to an increase in the electroluminescence (EL) quantum efficiency of the device. Here, we demonstrate a relationship between the EL emission linewidth and $\Delta V_{OC, nr}$ in a set of polymer-nonfullerene blends. Based on this finding, we achieved an extremely low $\Delta V_{OC, nr}$ of 155 mV using an aggregation-less PM6:Y16F blend and subsequently fabricated a near-infrared light-emitting device that is among the best reported fluorescent OLEDs in 900 nm. This work indicates that design of new acceptors with narrow emission linewidths is essential to further enhance the performance of both NIR-OLEDs and OSCs.

and the energy of the interfacial charge-transfer (CT) states is very close that of the NFA local exciton (LE). As a result, the emission spectrum and absorption tails consist of contributions of CT, LE, and CT-LE hybrid states, or mid-gap trap states,[16] which are, however, difficult to distinguish from each other.[17–19] Moreover, their emission quantum yield, and thus the resulting $\Delta V_{OC,nr}$ for a given D:A combination, has been shown to depend on the interfacial morphology[9,20,21] and molecular packing behavior,[22] causing variations in $\Delta V_{OC,nr}$ in the range of 50–300 mV, i.e., changes in EQE_{EL} within a factor of about 10^1–10^5 according to Equation 1. In order to increase the PCE of OSCs, but also to enable NIR-OLEDs, it is of great importance to understand the molecular and morphological sources for nonradiative recombination in these low-energy-offset D:A blends.

The nonradiative decay rate is related to molecular vibrations and electron-phonon coupling by the energy-gap law and theoretical models predict that the same parameters affect the fine structure and shape of the low-energy part of the emission spectrum.[23] In this work, we explore this relation and study a set of efficient polymer-NFA blends with different energy-level offsets and blend morphologies. We find that the blends with larger offsets or lower neat NFA emission quantum yields have a broader electroluminescence (EL) emission spectrum. We further observe a broadening when a more strongly aggregated blend morphology is achieved for a certain D:A combination. In general, we find that the linewidth of the EL spectrum correlates strongly with $\Delta V_{OC,nr}$.

Based on these findings, and with the aim of reducing $\Delta V_{OC,nr}$ to unprecedented values, we designed blend combinations with an aggregation-less morphology using low-molecular-weight fractions of the polymer PM6 (poly[(2,6-(4,8-bis(5-(2-ethylhexyl-3-fluoro)thiophen-2-yl)-benzo[1,2-b:4,5-b']dithiophene))-alt-(5,5-(1',3'-di-2-thienyl-5',7'-bis(2-ethylhexyl)benzo[1',2'-c:4',5'-c']dithiophene-4,8-dione)]). This enables emission linewidths for the blends as narrow as the neat NFA materials and $\Delta V_{OC,nr}$ values for the resulting OSCs down to 155 mV. These devices have their emission peaks in the 850–950-nm range and reach EQE_{EL} values of up to 0.52%, with a remarkably low onset voltage (5 mA/cm² at 1.2 V). This makes the NFAs currently used in the best OSCs among the best emitters in NIR-OLEDs, with record conversion efficiencies of electrical power to NIR optical power (PCE_{LED}) in the 900-nm range. These findings emphasize that a narrow emission linewidth, high EQE_{EL}, low $\Delta V_{OC,nr}$ and low emission-onset voltage are strongly related and that future research on NIR-OLEDs and OSCs should go hand in hand.

RESULTS AND DISCUSSION

Electroluminescence properties of low energetic offset polymer: NFA blends

For this study, we carefully chose a set of polymer-NFA combinations consisting of two well-known polymers (PTB7-Th and PM6) and three NIR light-absorbing nonfullerene acceptors with similar optical gaps (E_{opt}), being FOIC,[24] Y6,[7] and its derivative Y16F.[9] Their chemical structures are shown in Figure 1A, alongside their electronic energy levels (Figure 1B) measured by cyclic voltammetry (CV) under the same conditions for all materials. Note that the HOMO energy levels derived from CV measurements on films (see section S2) are likely to be slightly altered in the blend films due to modified molecular packing or morphology as compared with neat materials. All devices were fabricated in an inverted architecture, namely glass/ITO/ZnO sol-gel/active layer/MoO₃/Ag. They comprise next to the D:A blends also neat NFA photoactive layers, all processed at room temperature, without thermal treatment from an additive-free chloroform solvent, unless mentioned otherwise. The

[1]UHasselt—Hasselt University, Institute for Materials Research, (IMO-IMOMEC), Agoralaan 1, 3590 Diepenbeek, Belgium

[2]IMOMEC Division, IMEC, Wetenschapspark 1, 3590 Diepenbeek, Belgium

[3]Lead contact

*Correspondence: quan.liu@uhasselt.be (Q.L.), koen.vandewal@uhasselt.be (K.V.)

https://doi.org/10.1016/j.joule.2021.06.010
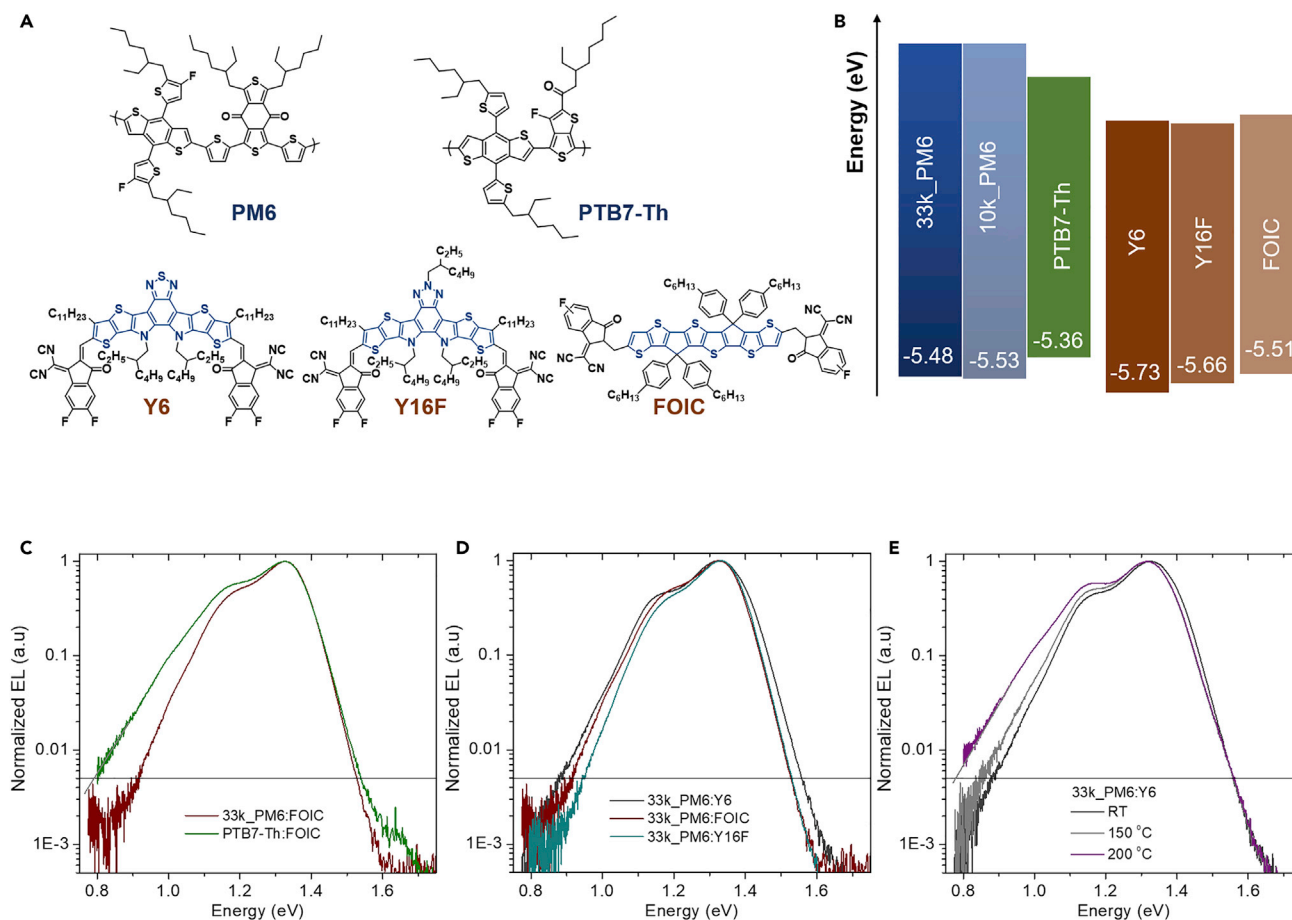
Figure 1. Low LE-CT energetic offset active material systems and their electroluminescence properties

(A) Molecular structures of the donor polymers and low-E_{opt} NFAs used in this study.

(B) Energy levels of the materials. See experimental details in section S2.

(C) Normalized EL spectra of devices based on PTB7-Th:FOIC and 33k_PM6:FOIC blends.

(D) Normalized EL spectra of 33k_PM6:Y6, Y16F and FOIC based solar cells.

(E) Evolution of the EL spectra for 33k_PM6:Y6 devices with varying preannealing temperatures for 15 min on the active layers.

processing conditions were not optimized for achieving the highest possible cell efficiency but enabled easy comparison within different blend systems. Also, note that the studied blends had negligible degradation when stored in a nitrogen-filled glovebox for several months (Table S2). All key parameters are summarized in Table 1, and the details of the photovoltaic parameters, EQE$_{PV}$, and EQE$_{EL}$ are shown in section S3.

We first consider the influence of the energy-level offset on the photovoltaic and emission properties. PTB7-Th yields the largest HOMO energy offset with FOIC, and PTB7-Th:FOIC devices yield a V_{OC} of 0.74 V, which is approximately 0.1 V less than that of PM6:FOIC cells. In both devices, no clear CT absorption is visible in the subgap region of the sensitively measured photovoltaic external quantum-efficiency (EQE$_{PV}$) spectra (Figure S5), and no obvious extra emission band is observed in the EL spectrum (Figure 1C), which at first sight resembles the emission spectrum of neat FOIC. The reduced V_{OC} in the case of PTB7-Th is therefore mainly due to increased $\Delta V_{OC,nr}$, which is in good agreement with the observation that the EQE$_{EL}$ of PTB7-Th:FOIC is about two orders of magnitude lower than that of the PM6:FOIC

Table 1. Summary of key parameters for the studied devices in this work

Active material	E_g/q (V)	V_{OC} (V)	PCE (%)	EQE$_{PV\ max}$ in NFA (%)	$E_g/q - V_{OC}$ (V)	$V_{OC,rad}$ (V)	Calc. $\Delta V_{OC,nr}$ (V)	Exp. EQE$_{EL}$	Exp. $\Delta V_{OC,nr}$ (V)
33k_PM6:Y6	1.41	0.837	15.4	82	0.57	1.085	0.248	6.3E-5	0.250
33k_PM6:Y6 (150°C)	1.39	0.805	15.2	85	0.58	1.071	0.266	2.6E-5	0.274
33k_PM6:Y6 (200°C)	1.39	0.739	11.5	84	0.65	1.067	0.328	2.6E-6	0.333
10k_PM6:Y6	1.42	0.910	7.6	66	0.51	1.095	0.185	1.0E-3	0.177
Y6	1.39	0.902	0.07	–	0.49	–	–	1.5E-3	0.167
PTB7-Th:FOIC	1.38	0.737	11.3	81	0.65	1.062	0.325	4.5E-6	0.318
33k_PM6:FOIC	1.38	0.845	7.5	50	0.54	1.064	0.219	2.6E-4	0.213
10k_PM6:FOIC	1.39	0.870	3.9	27	0.52	1.071	0.201	7.1E-4	0.187
FOIC	1.37	0.872	0.15	–	0.50	–	–	1.0E-3	0.178
33k_PM6:Y16F	1.39	0.881	12.2	74	0.50	1.076	0.195	6.8E-4	0.188
10k_PM6:Y16F	1.39	0.922	5.2	49	0.47	1.080	0.158	2.5E-3	0.155
10k_PM6:Y16F (1.5:1)	1.41	0.953	2.23	30	0.46	1.099	0.146	3.6E-3	0.145
10k_PM6:Y16F (3:1)	1.43	0.980	1.05	16	0.45	1.120	0.140	5.0E-3	0.137
Y16F	1.37	0.889	0.03	–	0.49	–	–	2.6E-3	0.154

The optical gap (E_{opt}) is determined from the intersection of the normalized EQE$_{PV}$ and EL spectra (Figure S7). The detailed photovoltaic parameters and EQE$_{EL}$ of the devices are summarized in Table S4 and Figure S6, respectively. Radiative open-circuit voltages ($V_{OC,rad}$) were calculated from the FTPS-EQE$_{PV}$ spectra (Figure S5) shown in section S3. Calculated nonradiative recombination (Calc. $\Delta V_{OC,nr}$) values of the devices are determined by $V_{OC,rad} - V_{OC}$[22] and experimental values (Exp. $\Delta V_{OC,nr}$) are directly obtained from $\Delta V_{OC,nr} \approx -\frac{k_B T}{q} \ln(EQE_{EL})$.

device (see EQE$_{EL}$ spectra in Figure S6). Such an increase in EQE$_{EL}$ upon minimizing the HOMO-energetic offset has been previously observed and explained by either a hybridization of the CT state with the emissive LE states[25] or a thermal equilibration between the LE and CT state.[19] Both mechanisms are expected to affect the spectral shape of the emission spectrum as compared with that of the neat material. Furthermore, the emission-line shape of the devices is strongly affected by self-absorption and optical interference (see Figures S9 and S11B).[26,27] For a fair comparison, we therefore made sure to control the thickness of the photoactive layers to be ca. 100 nm and defined the emission linewidth based on the log scale spectra as shown in Figures 1C–1E: the difference between the photon energies where the value of the normalized emission spectrum reaches 5×10^{-3} (gray line in Figures 1C–1E) is taken as a measure to indicate the width of the emission spectrum. Note that this measure ΔE_{5E-3} is much more affected by the emission tail at lower energies (see Figures 1C and 1E) than, for example, the full width at half maximum, and gives the best correlation with $V_{OC,nr}$ of all the studied OSCs (Figure S10) and later shown in Figure 4D.

Going back to the EL spectra of PM6:FOIC and PTB7-Th:FOIC, shown in Figure 1C, we observe a much larger ΔE_{5E-3} in the case of PTB7-Th, which has the larger HOMO offset. A similar observation is made in Figure 1D, which shows a larger ΔE_{5E-3} for PM6:Y6 as compared to PM6:FOIC. The latter has 0.2 eV less HOMO offset and a higher EQE$_{EL}$, even though a device containing neat FOIC has a lower EQE$_{EL}$ than for neat Y6 (see Table 1 and Figure S6). The PM6:Y16F-based devices show the smallest ΔE_{5E-3} of the D:A combinations described so far, as well as the highest EQE$_{EL}$ (Table 1). We attribute the lower ΔE_{5E-3} for the Y16F devices to the fact that the Y16F LE has a narrower emission linewidth than the Y6 LE. In fact, in devices comprising neat NFA active layers, Y16F has the highest EQE$_{EL}$ (Table 1; Figure S6).

We now turn our attention to morphological and aggregation effects affecting the emission properties. It is known that aggregation in blends has an influence on the frontier orbital energy levels[28] and thus on the degree of LE/CT hybridization and/or the LE/CT population equilibrium, as well as the voltage losses. In Figure 1E,

EL spectra of PM6:Y6 devices for various thermal annealing temperatures are shown. Clearly, ΔE_{5E-3} increases with increasing temperature. The device annealed at 200°C is expected to have the largest extent of polymer and NFA aggregation and yields the broadest EL spectrum and the largest $\Delta V_{OC,nr}$, over 80 mV larger than for the as-cast film (Table 1). As will be shown in the next section, these thermally induced nanomorphology changes are confirmed by atomic force microscopy (AFM) measurements.

Strategy for reducing $\Delta V_{OC,nr}$ for low energetic offset PM6:NFA solar cells

Inspired by the observation that an increased D:A intermixing and reduced aggregation narrows the emission spectrum and increases EQE_{EL}, we have synthesized low-molecular-weight PM6 polymer batches with the aim of manipulating the interfacial energy landscape and nonradiative recombination rate. For this purpose, a dedicated droplet-flow-polymerization protocol was applied. Details on the synthesis procedure are given in section S1. To examine the degree of intramolecular packing of the PM6 polymer, we recorded temperature-dependent absorption spectra of the various molecular-weight fractions in a chloroform solution. As shown in Figure 2A, the standard PM6 with a number-average molar mass (M_n) of 33 kDa exhibits a pronounced shoulder at 615 nm, which only slightly reduces as the temperature increases, indicating an intrinsically strong aggregation of the polymer chains both in solution and in the solid state.[29,30] For the PM6 batches with reduced M_n, a large decrease of such shoulder peaks was observed together with a gradual blue shift in absorption and a decrease of intensity with increasing temperature, suggesting that the low-M_n polymers are very weakly aggregated in solution. This dependence of the aggregation state on M_n is hypothesized to result in PM6:NFA films with varying degrees of intermixing or aggregated nanomorphology, schematically shown in Figure 2B. Morphology studies for all PM6:NFA blend films support this picture: as shown in Figures 2D, 2E, S8A, S8B, S8D, and S8E), AFM height and phase images suggested an obvious phase separation with well-distributed fiber-like aggregation textures in the high-M_n blend systems. In contrast, such aggregation patterns were almost invisible or weakened in the low-M_n blend systems, indicating a more D/A intermixed nanomorphology. Furthermore, when the high-M_n PM6:Y6 blend was subjected to 200°C thermal annealing, the aggregates become more clearly visible (Figure 2C). Transmission electron microscopy (TEM) images (Figures 2F, S8C, and S8F) further support these observations: The uniformly distributed flower-like phase separation (indicative of aggregate morphology[31]) in all high-M_n blends disappears or greatly reduces in their low-M_n counterparts.

Decreasing M_n improves the V_{OC} in the three studied blend systems, with the measured J-V curves shown in Figures 3A–3C. The increase in V_{OC} is largest for the PM6:Y6 blend, approximately 75 mV when going from an M_n of 33 to 10 kDa. A further reduction in M_n does not significantly improve the V_{OC}. We note that such large V_{OC} enhancement does not originate from reduced surface recombination or trap-assisted recombination in the bulk heterojunction (BHJ) blend[32] since negligible changes were observed in the blend surface roughness (AFM images in Figures 2 and S8), and in the slope of the semilogarithmic plot of the V_{OC} against light intensity (Figure S15). We therefore attribute such enhancement to a reduction in HOMO-energetic offset between PM6 and Y6 when low-Mn polymer was used (B). Additionally, the well-intermixed blend morphology reduces polymer aggregation and further lowers the HOMO level.[33,34] The reduced $\Delta V_{OC,nr}$ agrees well with the EQE_{EL} measurements (Figure S6), and EQE_{EL} values in the low-M_n polymer based cells reach similar values as those of devices fabricated with the respective neat NFA materials. Furthermore, narrower EL spectra, shown in Figures 3D–3F, were
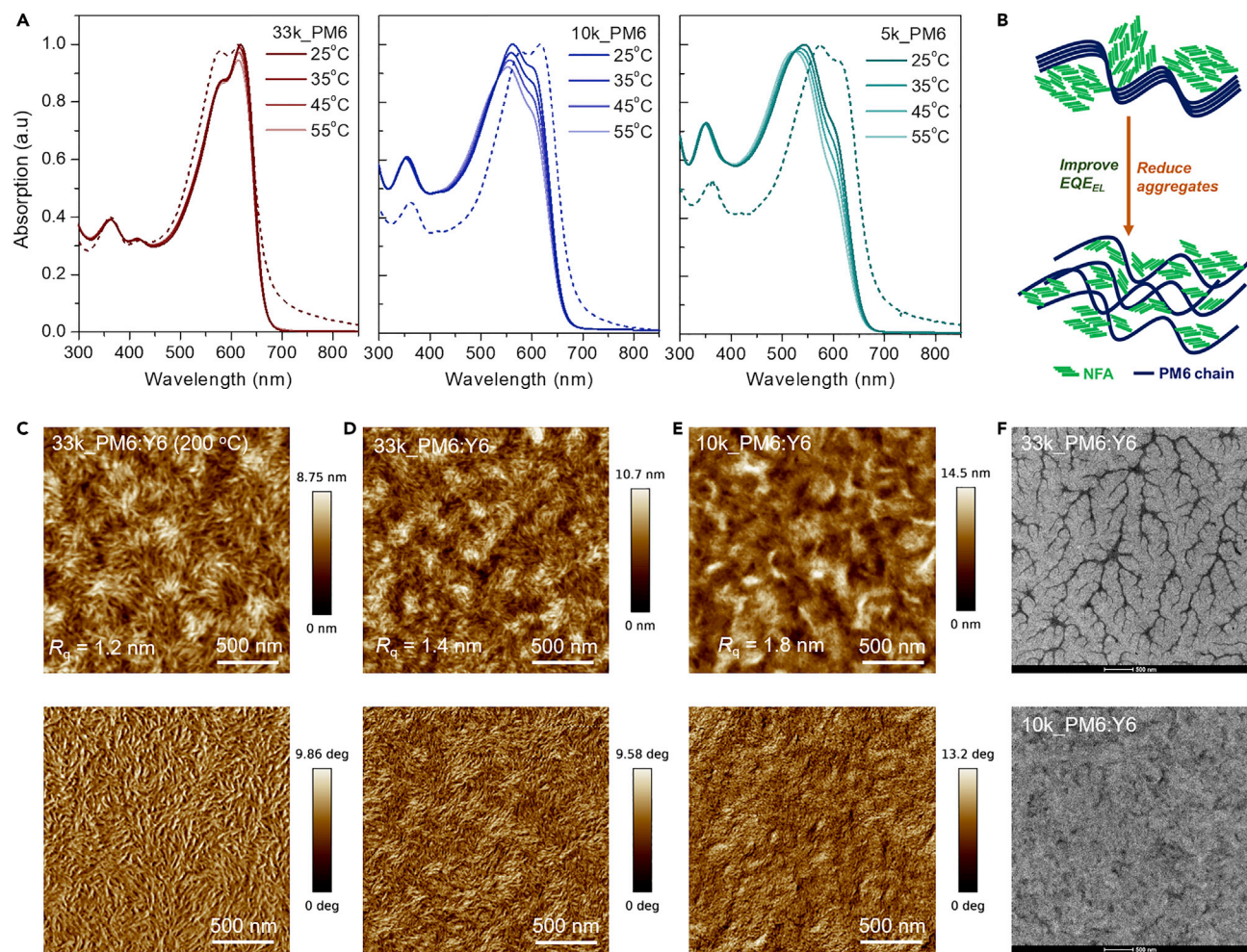
Figure 2. Construction of blend films with reduced aggregates and morphology characterization

(A) Temperature-dependent absorption spectra for different molecular-weight batches of PM6 in chloroform solution. The dotted spectra stand for thin films.

(B) Schematic drawing of the possible nanomorphology evolution in the PM6:NFA blends. At the top, high-M_n polymer chains induce large aggregates for both PM6 and the NFA, while at the bottom, the low-Mn polymer increases the intermixing of the two phases by reducing their self-aggregation. (C–E) Atomic force microscopy (AFM) images of the 200°C thermally annealed 33kPM6:Y6, as-cast 33kPM6:Y6, and 10kPM6:Y6 blend films on ITO/ZnO substrates, respectively. Top: height images. Bottom: phase images.

(F) Transmission electron microscopy (TEM) images of the as-cast 33kPM6:Y6 (top) and 10kPM6:Y6 (bottom) blend films.

measured for the low-M_n polymer devices and their linewidths are comparable with those of pure NFA-based devices (Figure 4A). The narrowed EL line shape indicates a suppressed nonradiative decay rate via molecular vibrations, as discussed later.

Even though the V_{OC} improves, the short-circuit current (J_{SC}) and fill factor (FF) are sacrificed, resulting in lower overall efficiencies for the lower-M_n blend systems. A summary of the molecular-weight-dependent photovoltaic performance is given in Figure S14. J_{SC} losses for the lower-M_n PM6:Y6 blends are associated with a decreased internal quantum efficiency (IQE) (Figure S16). We mainly attribute this to a reduced exciton-dissociation efficiency. The photoluminescence (PL) in NFA is approximately 30% less quenched in the lower-M_n blend film, as shown in Figure S17, which is consistent with a J_{SC} reduced from 25.4 to 19.2 mA/cm². The reduced FF correlates with a reduced hole mobility. By decreasing M_n from 33k to
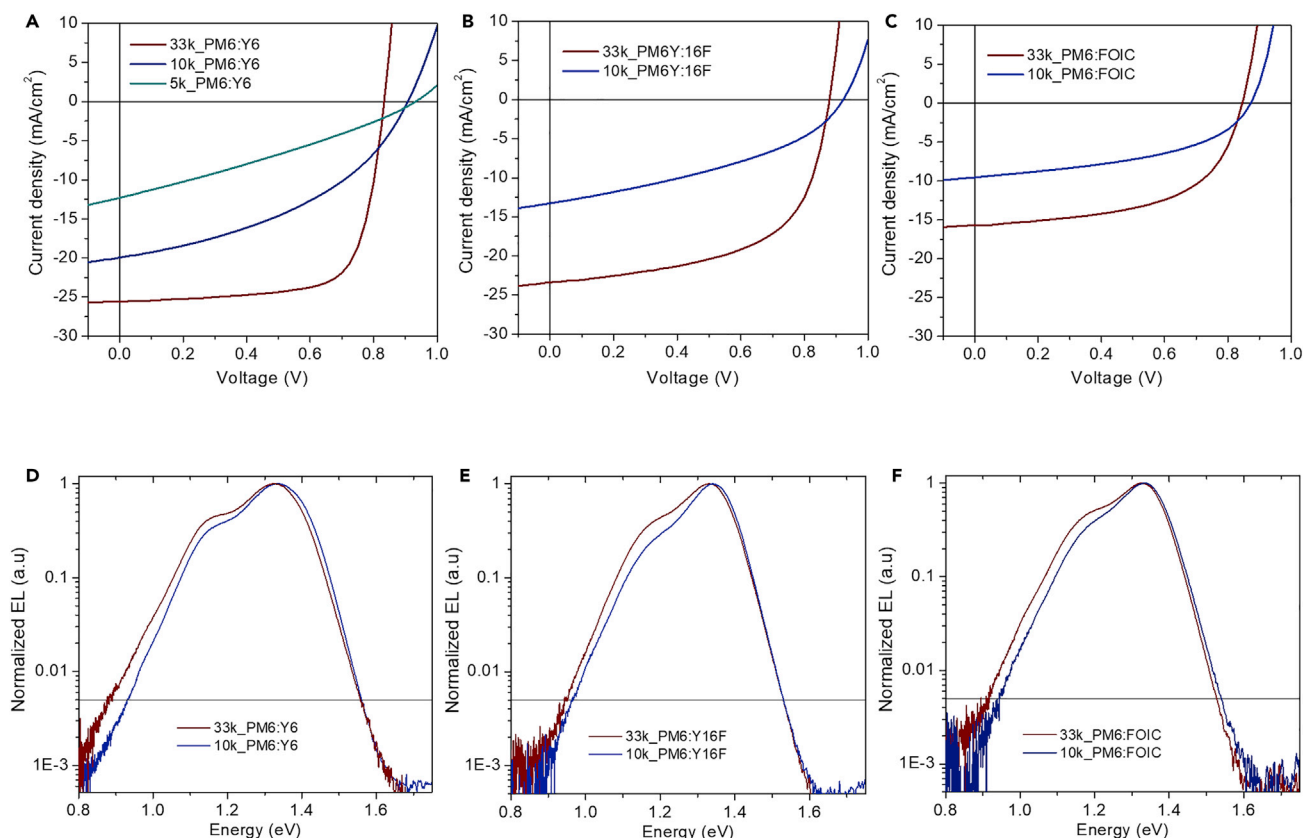
Figure 3. Low-molecular-weight blends with less-aggregation morphology minimize nonradiative recombination losses
(A–C) J-V curves of solar cells based on high- and low-M_n PM6:NFA blends measured under AM1.5G sunlight at 100 mW/cm^2.
(D–F) Normalized EL spectra (eV) corresponding to (A–C), respectively.

10 kDa in the PM6:Y6 blend, electron mobilities remain unchanged while hole mobilities were reduced by more than one order of magnitude (Figure S18).

To further improve OSCs, that is, to surpass the 20% efficiency barrier in particular, EQE$_{EL}$ enhancement should be achieved simultaneously with high IQE and high FF. Previous work has shown that the trade-off between IQE and energetic offsets for current low-band-gap NFA cells[35,36] can be overcome by increasing the exciton lifetimes of the low-gap NFA materials.[19] Moreover, a well-designed blend morphology with high and balanced mobilities is essential to maintain high FF, as well.

Correlation between nonradiative recombination loss and EL linewidth
Summarizing all data from the experiments on low-energy-offset polymer:NFA blends described above, a correlation can be seen between $\Delta V_{OC,nr}$ and ΔE_{5E-3}. This clearly indicates that in our quest for high-efficiency OSCs, we should focus on those D:A blends, and hence neat materials, with the narrowest emission spectra.

We propose two possible origins for this remarkable observation. Even though no distinct CT emission band is observed, the anticipated slightly lower energy of the CT states might introduce, in addition to neat NFA emission, some extra low-energy emission, hereby broadening the spectra. Since CT states are less emissive than the neat LE of the NFA, a lower EQE$_{EL}$ is indeed expected.[37] However, this does not
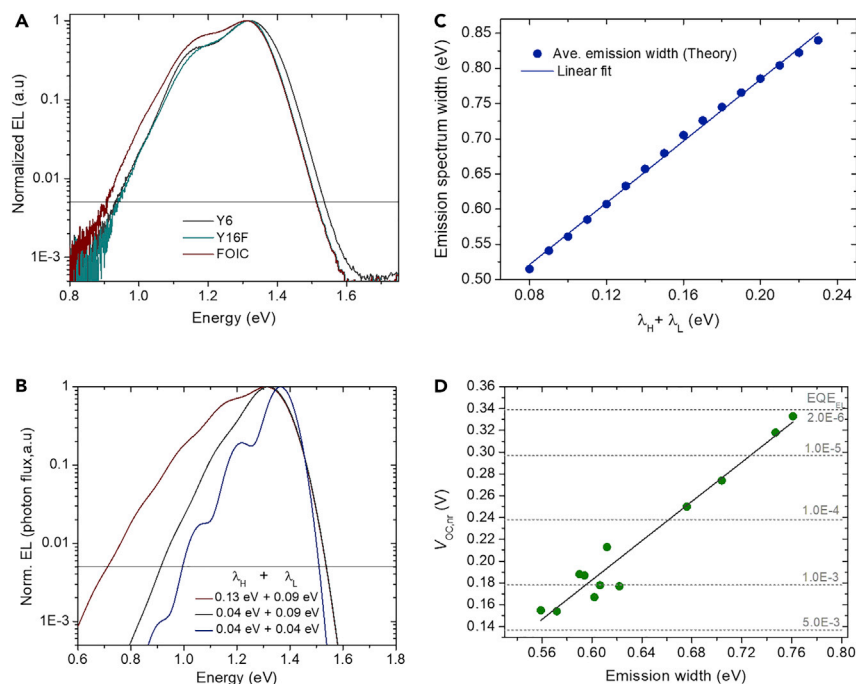
Figure 4. Correlation of the emission spectrum width with EQE_EL

(A) Measured EL spectra of neat NFA-based devices with similar thicknesses as the blends used for solar cells.

(B) Computed EL spectra with a set of reorganization energies: E_s = 1.40 eV, E_h = 0.15 eV, λ_H = 0.4–0.9 eV, and λ_L = 0.5–1.3 eV.

(C) Plot of the calculated spectrum width as a function of reorganization energies. The solid line presents the best linear fit for the computed data.

(D) Correlation between the emission spectrum width (see details in Table S5) and nonradiative recombination voltage losses of all the studied devices. Relevant EQE_EL values are indicated as gray solid lines. The black solid line presents the best linear fit of the experimental data.

explain why the different neat NFAs have different EQE_EL values. In fact, the EQE_EL of the neat NFA devices also correlates with $\Delta E_{5E\text{-}3}$, as shown in Figure 4A, with Y16F having the smallest $\Delta E_{5E\text{-}3}$ and the best EQE_EL among the three studied NFA materials.

The lineshape of the emission spectrum can be related to the excited state energy E_S and high- and low-frequency reorganization energies, λ_H and λL, respectively. The line shape of the spectral flux of emitted photons N_{ph} is given by Equation 2.[23]

$$N_{ph} \sim E^3 \sum_{n=0}^{+\infty} \frac{\exp(-S)S^n}{n!} \exp\left(-\frac{(E - E_S + \lambda_L + nE_h)^2}{4\lambda_L kT} \right) \qquad \text{(Equation 2)}$$

where E_h is the vibronic spacing and $S = \lambda_H/E_h$ the Huang Rhys factor. The parameters in Equation 2 also determine the nonradiative decay rate, which is proportional to the reduced emission spectrum (N_{ph}/E^3) evaluated at a photon energy E of 0.[23]

Figure 4B shows calculated emission spectra for an E_S of 1.40 eV, which is close to the gap of all three studied NFA materials, a typical E_h of 0.15 eV and selected values for λ_H and λ_L. Low-finesse optical cavity (ITO-Ag) effects, together with a significant increase in ITO reflection for wavelengths larger than 1,000 nm (Figure S11A) make it difficult to perform an accurate fitting of the measured emission spectra with Equation 2. We also note that the measured linewidth of the EL spectra are narrower than

that of steady PL spectra because the emission intensity enhances in the cavity resonance region, while being suppressed in the off-resonance region (Figure S13)[27]. Furthermore, the simplicity of Equation 2 might not accurately capture all physical effects responsible for the broadening of the emission spectrum. However, a comparison between the curves following Equation 2 and the experimental curves shows that all main features of the emission spectra present in the simple model are also experimentally observed (Figures 4A and 4B). We can state that the width of the EL spectrum, as defined by $\Delta E_{5E\text{-}3}$, correlates with the total reorganization energy, which in the case of the simple model in Equation 2 is the sum $\lambda_L + \lambda_H$. This is shown in Figure 4C, illustrating a linear relationship between $\Delta E_{5E\text{-}3}$ determined for selected curves following Equation 2 and the total reorganization energy.

In Figure 4D, the $\Delta V_{OC,nr}$ of all the studied devices based on blends and pure NFAs is plotted as a function of $\Delta E_{5E\text{-}3}$. The correlation between these two quantities implies that a smaller total reorganization energy results both in narrower emission spectra and smaller nonradiative losses. Furthermore, we have shown in the previous paragraph that properly designed OSCs can have an emission linewidth and EQE_{EL} very close to those of the pure NFA material. The aggregation-less polymer:NFA blends demonstrated in this study are examples of the latter.

Performance of polymer:NFA devices as near-infrared OLEDs

For the D:A combinations studied in this work, we have observed that the IQE is sacrificed when an OSC blend has the emission properties of the neat NFA material. Even though the V_{OC} is increased, this leads to a lower overall photovoltaic performance (Table S4). However, as the V_{OC} of the devices increases and approaches the radiative limit, the D:A blends are expected to be good LEDs, demonstrating a high EQE_{EL}. In fact, very recently, a bifunctional OLED-OPV device emitting ~700 nm was demonstrated using a wide-band-gap NFA blend, exhibiting 0.2% EQE_{EL}, as well as 26% PCE under indoor-illumination conditions from a 1,000 lux LED.[38] This is a new type of organic optoelectronic, which has not been extensively studied. New fundamental working mechanisms different from classical fluorescent OLEDs are, however, expected: Their emission is based on hybrid local and charge-transfer states (HLCT). While not many studies have been performed on the exact working mechanism, exciton utilization efficiency values could break the spin-statistics limit of 25% since CT states and fluorescent excitons, as well as free charge carriers are all close in energy and can convert into one another.

While OLEDs with EQE_{EL} values reaching over 30% have been achieved in the visible spectral region,[39–44] achieving high-performance devices has been proportionally more difficult with increasing design wavelength due to the energy-gap law. The best reported NIR-OLEDs in the 900–950 nm range, based on triplet 5-(2-pyridyl) pyrimidinate Pt(II) complexes, do not have an EQE_{EL} larger than 2.1%.[45] The PM6:Y16F system described above is actually among the best NIR-OLEDs within the spectral region beyond 900 nm, based on fluorescent organic materials[46] (see Table S7), even though Y16F was designed as an OSC material and not specifically as a NIR-OLED material.

To further improve the light-emitting properties, we dispersed Y16F molecules into the small-molecular-weight PM6 ($M_n \approx 10$ kDa) host material at a lower concentration than in the OSC devices (1:1.2) to prevent exciton self-quenching in the blended emitting layer. Their thin-film absorption, steady PL, and estimated PL quantum efficiencies are shown in Figure S19. The strongest EL intensity observed under the same injected current was from devices emitting at 890 nm in which a PM6:Y16F
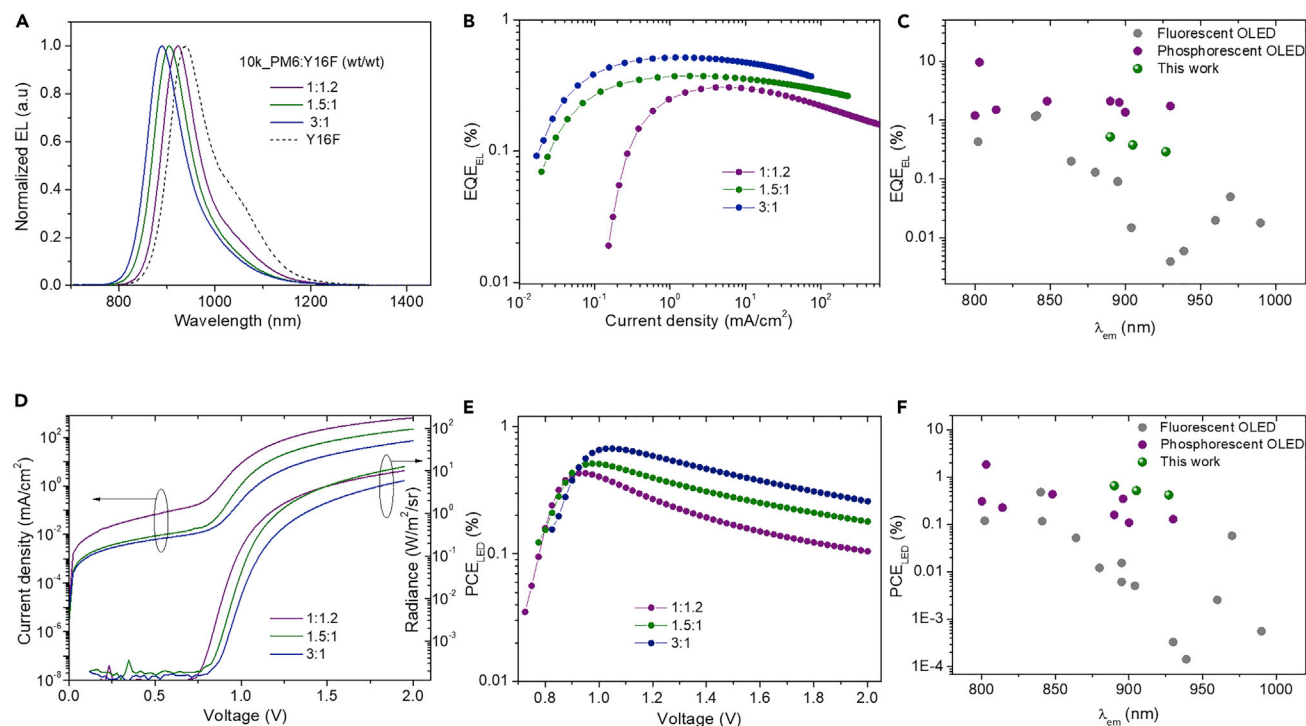
Figure 5. Performance of near-infrared OLED devices

(A) Electroluminescence spectra of 10k_PM6:Y16F-based OLED devices with different weight ratios (injected current = 1 mA).

(B) EQE_{EL} of the devices plotted against the injected current density.

(C) EQE_{EL} plotted against literature values with reported EL emission peaks ranging from 800 to 1,000 nm.

(D) J-V-R curves showing turn-on voltages are lower than 0.9 V.

(E) PCE of devices with applied voltage bias. $PCE_{LED} = EQE_{EL} \times h\nu/eV$, where $h\nu$ is the energy of the emitted photons, e is the elementary charge, and V is the voltage applied to the devices.

(F) PCE comparison with NIR-OLEDs reported in literature.

blend with a weight ratio of 3:1 was used (Figure 5A). A blue shift in the EL signal from the devices is seen as the Y16F concentration is reduced, which we attribute to the diminished Y16F molecular aggregation in the blended films. Figure 5B shows EQE_{EL} as a function of injected current density for the devices, with the highest EQE_{EL} achieved being 0.52%, which is two times larger than that of the neat Y16F device. We note that, in comparison with literature reported NIR-OLEDs with an emission peak maximum from 800 to 1,000 nm (see Table S7), our highest performing NIR-OLED device outperforms most of the fluorescent OLEDs, with only a few exceptions (Figure 5C) and approaches the best-performing heavy-metal-based phosphorescent NIR-OLEDs. In the optimized 3:1 NIR-OLED, we measured a V_{OC} as high as 0.98 V for an optical gap of 1.43 eV, resulting in a voltage loss of 0.46 V and a $\Delta V_{OC,nr}$ below 0.14 V, which is in good agreement with the theoretically calculated value using Equation S1 (see section S3; detailed EQE_{PV} and photovoltaic parameters are shown in section S7).

As compared with other previously reported types of NIR-OLED materials such as fluorescent host-guest systems, vacuum-processed phosphorescent metal-based complexes, or thermally activated delayed fluorescence (TADF) emitters, the design using polymer donor-acceptor organics allows for simple, cost-effective fabrication, is free of heavy metals, and permits lower onset voltages of emission.[47,48] This is beneficiary as it allows to achieve a high radiance at a lower voltage, thus resulting in a higher conversion efficiency of electrical power into optical power. The current

density-voltage-radiance (*J-V-L*) characteristics of the PM6:Y16F OLED devices are shown in Figure 5D. All NIR-OLEDs fabricated feature low turn-on voltages of less than 1.0 V for a measurable photon output, although a slight increase was found when the Y16F concentration in the blend decreases. The high EQE_{EL} recorded in the lower concentration blend devices, taken together with the low driving voltages, result in a high PCE_{LED}. As shown in Figure 5E, the optimal device performs with a peak PCE as high as 0.66%, a significant improvement over the values of recently reported best-performing NIR-OLEDs based on phosphorescent Pt(II) (supplemental reference S14) and TADF (supplemental reference S17) emitters with similar emission peak (see PCE_{LED} comparison in Figure 5F and Table S7).

Conclusion

We have experimentally observed a correlation between EL linewidth, EL quantum efficiency, and nonradiative voltage losses in several systems with low energetic offsets between polymer donors and NFA acceptors, in which the emission spectra are dominated by the properties of the low-gap NFAs. The emission properties are varied by varying the HOMO energy-level offset between the polymer and NFA, the emission quantum yield of the NFA, and the tuning of the blend morphology. Our observations show that in these systems, both the nonradiative decay rate and the EL linewidth are affected similarly by molecular properties, being the reorganization energy and the possible presence of very weakly emitting CT states with an energy slightly below that of the local NFA exciton. Based on this, a reduced $\Delta V_{OC,nr}$ was successfully achieved by using low-molecular-weight PM6 polymer with a designed aggregation-less blend morphology and minimized HOMO offset with the NFAs FOIC, Y6, and Y16F. The smaller $\Delta V_{OC,nr}$ of OSCs thus corresponds to a narrower EL emission width, which is comparable with their pure NFA counterpart. Considering the low $\Delta V_{OC,nr}$, particularly in the PM6:Y16F blend, we further demonstrated solution-processable heavy-metal-free OLEDs that achieve EL in the 890–930-nm range by optimizing the Y16F concentration in the blend. The optimal EQE_{EL} is among the best reported fluorescent NIR-OLEDs that emit in the 900-nm range. Furthermore, when power efficiency is considered, we achieved a PCE_{LED} that outperforms currently reported NIR-OLEDs in the wavelength range above 850 nm as a result of the low emission-onset voltage. We therefore conclude that in order to reach increased efficiencies for both NIR-harvesting OSCs and NIR-OLEDs, novel low-gap organic semiconductors with narrow EL emission linewidths, which are indicative of low reorganization energies, are essential.

EXPERIMENTAL PROCEDURES

Resource availability

Lead contact

Further information and requests for resources and materials should be directed to and will be fulfilled by the lead contact, Koen Vandewal (koen.vandewal@uhasselt.be).

Materials availability

The materials in this study will be made available on request.

Data and code availability

The published article includes all data generated or analyzed during this study.

Materials and solution preparation

The polymer PM6 ($M_n \approx$ 33 and 20 kDa) and the nonfullerene acceptors (Y6, Y16F and FOIC) were purchased from 1-material. PTB7-Th was purchased from Solaris

Chem. Low-M_n PM6 polymer batches ($M_n \approx$ 10 and 5 kDa) were synthesized at Hasselt University using a dedicated continuous droplet-flow-polymerization procedure.[49] Experimental details are shown in section S1. All materials were used as received without further purification. The sol-gel ZnO precursor (0.45 M) was prepared by dissolving zinc acetate dehydrate (Aldrich, 99.9%, 0.5 g) and ethanolamine (Aldrich, 99.5%, 0.14 g) in 2-methoxyethanol (Acros Organics, 99.8%, 5 mL).[50] To complete the hydrolysis reaction, this solution was vigorously stirred at 60°C for 2 h and then stirred at room temperature for 12 h in air. Solutions of PM6:NFA, PTB7-Th:FOIC and pure NFA at a total concentration of 11–16 mg/mL (donor/acceptor = 1:1.2 wt/wt in all the blends) were prepared in chloroform and stirred at 50°C for 2 h in a N_2-filled glovebox before use.

Device fabrication

OSCs and NIR-OLEDs were fabricated using the same inverted device structure glass/ITO/ZnO/Active layer/MoO$_3$/Ag. We firstly spin-coated the ZnO precursor solution on pre-cleaned and UV-Ozone treated ITO (Biotain Crystal, 15 Ω sq^{-1}) substrates and it was annealed at 180°C in air for 20 min to form a 30 nm electron-transporting layer. The prepared samples were then transferred into a N_2-filled glovebox for spin-coating the active layer with controlled thicknesses (90–100 nm) by adjusting the spin-casting rate. The blend thickness was monitored by a Bruker Veeco Dektak XT profilometer. Finally, the MoO$_3$ (10 nm) hole-transporting layer and the Ag (100 nm) electrode were sequentially deposited on the active layer through a shadow mask by thermal evaporation (<5 × 10^{-6} mbar) with an area of 0.06 cm^2. The freshly fabricated devices were encapsulated with glass slides using an UV-curable epoxy (DELO-LP655) in the glovebox and measured in air. J-V curves (forward scan with a step of 25 mV) were recorded using a Keithley 2400 Source meter under AM1.5 1-sun illumination provided by a solar simulator (Newport 91195A) with an intensity equivalent to 100 mW cm^{-2}, which was calibrated with a silicon reference cell. The EQE$_{PV}$ spectrum for each cell was measured under chopped (135 Hz) monochromatic illumination from a Xe lamp (100 W, Newport) modulated by Cornerstone 130 Monochromator and an optical wheel chopper. The generated photocurrent from the solar cells was amplified with a Stanford Research System Model SR830 lock-in amplifier, and a calibrated Si photodiode with known spectral response was used as a reference.

FTPS-EQE and EQE$_{EL}$ measurements

FTPS-EQE measurements were performed using a INVENIO R (Bruker Optics) with an external detector. A low-noise current amplifier was used to amplify the photocurrent generated under illumination of the devices, with the illumination light modulated by the Fourier-transform infrared (FTIR) setup. The EQE$_{EL}$ was recorded with a home-built setup using a 100 mm^2 Hamamatsu silicon photodiode, which was placed directly in front of the device with a distance of 12 mm. A Keithley 2400 source meter was used to supply voltage and record the injected current, and simultaneously another Keithley 2400 was used to measure the emitted photons from the device. The radiance of the OLEDs was estimated using the same EQE$_{EL}$ setup and Lambertian emission was assumed. The thickness of the glass substrate was considered when calculating the solid angle.

Electroluminescence measurements

The EL emission spectra were recorded using an Andor spectrometer (Kymera 328i-D2-SIL) with an InGaAs array detector (DU490A-1.7), which was cooled to −60°C. An 830-nm long-pass filter was used to exclude the presence of peaks originating from the second order of diffraction from the grating. The voltage bias was applied to

devices with a Keithley 2400 external current/voltage source meter. The injected current was close to J_{SC} of OSC devices measured under AM1.5G illumination at 100 mW/cm^2, except the low EQE$_{EL}$ PTB7-Th:FOIC and 200°C thermally annealed 33k_PM6:Y6 cells, in which the injected current is approximately 3 times the J_{SC}. We further provided the injection dependent EL spectra of PTB7-Th:FOIC and 200°C thermally annealed 33k_PM6Y6 cells in Figure S12. That figure makes clear that the EL shape of the spectra remains unchanged when going from an injection current close to 1*J_{SC} (~1.6 mA) to 3* J_{SC} (~5 mA). The details of injection current density and applied voltages were also indicated in the supplemental information, see Table S5. The system was wavelength-calibrated by an argon lamp (HG-2, Ocean Optics) with a resolution better than 0.5 nm and irradiance-calibrated by a National Institute of Standards and Technology (NIST) calibrated light source (Ava-Light-HAL-CAL-Mini, 300–2,500 nm). For recovering the high-energy tail part of the EL spectra, a CCD silicon array detector (DU416A-LDC-DD) with a 590-nm long-pass filter was used (see Figure S9).

Morphology characterization

TEM was performed with a Tecnai G2 Spirit Twin. The TEM samples are identical to the active layers of the solar cells, spin-coated on glass/PEDOT:PSS substrates, subsequently floated off on a copper TEM grid (3.05 mm diameter, 400 mesh) in DI-water. Bright field TEM images were recorded with a magnification of 30 kx. AFM measurements were performed with a JPK/Bruker Nanowizard 3 in tapping mode.

SUPPLEMENTAL INFORMATION

Supplemental information can be found online at https://doi.org/10.1016/j.joule.2021.06.010.

AUTHOR CONTRIBUTIONS

Q.L. performed the core of the experimental work; S.S. synthesized low-molecular-weight PM6 polymers under the supervision of W.M.; S.M. and Y.X. helped with EL, PL, and FTPS-EQE measurements; A.V. performed AFM measurements, and J.D. measured the TEM samples. Q.L. and K.V. wrote the manuscript with assistance from all other authors.

DECLARATION OF INTERESTS

The authors declare no competing interests.

REFERENCES

1. Caspar, J.V., and Meyer, T.J. (1983). Application of the energy gap law to nonradiative, excited-state decay. J. Phys. Chem. *87*, 952–957.

2. Rau, U. (2007). Reciprocity relation between photovoltaic quantum efficiency and electroluminescent emission of solar cells. Phys. Rev. B *76*, 085303.

3. Benduhn, J., Tvingstedt, K., Piersimoni, F., Ullbrich, S., Fan, Y., Tropiano, M., McGarry, K.A., Zeika, O., Riede, M.K., Douglas, C.J., et al. (2017). Intrinsic nonradiative voltage losses in fullerene-based organic solar cells. Nat. Energy *2*, 17053.

4. Qian, D., Zheng, Z., Yao, H., Tress, W., Hopper, T.R., Chen, S., Li, S., Liu, J., Chen, S., Zhang, J., et al. (2018). Design rules for minimizing voltage losses in high-efficiency organic solar cells. Nat. Mater. *17*, 703–709.

5. Armin, A., Li, W., Sandberg, O.J., Xiao, Z., Ding, L., Nelson, J., Neher, D., Vandewal, K., Shoaee, S., Wang, T., et al. (2021). A history and perspective of non-fullerene electron acceptors for organic solar cells. Adv. Energy Mater. *11*, 2003570.

6. Li, C., Zhou, J., Song, J., Xu, J., Zhang, H., Zhang, X., Guo, J., Zhu, L., Wei, D., Han, G., et al. (2021). Nonfullerene acceptors with branched side chains and improved molecular packing to exceed 18% efficiency in organic solar cells. Nat. Energy. https://doi.org/10.1038/s41560-021-00820-x.

7. Yuan, J., Zhang, Y., Zhou, L., Zhang, G., Yip, H.-L., Lau, T.-K., Lu, X., Zhu, C., Peng, H., Johnson, P.A., et al. (2019). Single-junction organic solar cell with over 15% efficiency using fused-ring acceptor with electron-deficient core. Joule *3*, 1140–1151.

8. Jiang, K., Wei, Q., Lai, J.Y.L., Peng, Z., Kim, H.K., Yuan, J., Ye, L., Ade, H., Zou, Y., and Yan, H. (2019). Alkyl chain tuning of small molecule acceptors for efficient organic solar cells. Joule *3*, 3020–3033.

9. Liu, S., Yuan, J., Deng, W., Luo, M., Xie, Y., Liang, Q., Zou, Y., He, Z., Wu, H., and Cao, Y. (2020). High-efficiency organic solar cells with low nonradiative recombination loss and low energetic disorder. Nat. Photonics *14*, 300–305.

10. Cui, Y., Yao, H., Zhang, J., Zhang, T., Wang, Y., Hong, L., Xian, K., Xu, B., Zhang, S., Peng, J., et al. (2019). Over 16% efficiency organic photovoltaic cells enabled by a chlorinated acceptor with increased open-circuit voltages. Nat. Commun. *10*, 2515.

11. Yu, R., Yao, H., Cui, Y., Hong, L., He, C., and Hou, J. (2019). Improved charge transport and reduced nonradiative energy loss enable over 16% efficiency in ternary polymer solar cells. Adv. Mater. *31*, e1902302.

12. Wang, Y., Wang, Y., Zhu, L., Liu, H., Fang, J., Guo, X., Liu, F., Tang, Z., Zhang, M., and Li, Y. (2020). A novel wide-bandgap small molecule donor for high efficiency all-small-molecule organic solar cells with small nonradiative energy losses. Energy Environ. Sci. *13*, 1309–1317.

13. Cui, Y., Yao, H., Zhang, J., Xian, K., Zhang, T., Hong, L., Wang, Y., Xu, Y., Ma, K., An, C., et al. (2020). Single-junction organic photovoltaic cells with approaching 18% efficiency. Adv. Mater. *32*, e1908205.

14. Zhan, L., Li, S., Xia, X., Li, Y., Lu, X., Zuo, L., Shi, M., and Chen, H. (2021). Layer-by-layer processed ternary organic photovoltaics with efficiency over 18%. Adv. Mater. *33*, e2007231.

15. Yan, T., Ge, J., Lei, T., Zhang, W., Song, W., Fanady, B., Zhang, D., Chen, S., Peng, R., and Ge, Z. (2019). 16.55% efficiency ternary organic solar cells enabled by incorporating a small molecular donor. J. Mater. Chem. A *7*, 25894–25899.

16. Zarrabi, N., Sandberg, O.J., Zeiske, S., Li, W., Riley, D.B., Meredith, P., and Armin, A. (2020). Charge-generating mid-gap trap states define the thermodynamic limit of organic photovoltaic devices. Nat. Commun. *11*, 5567.

17. Eisner, F.D., Azzouzi, M., Fei, Z., Hou, X., Anthopoulos, T.D., Dennis, T.J.S., Heeney, M., and Nelson, J. (2019). Hybridization of local exciton and charge-transfer states reduces nonradiative voltage losses in organic solar cells. J. Am. Chem. Soc. *141*, 6362–6374.

18. Xu, Y., Yao, H., Ma, L., Hong, L., Li, J., Liao, Q., Zu, Y., Wang, J., Gao, M., Ye, L., and Hou, J. (2020). Tuning the hybridization of local exciton and charge-transfer states in highly efficient organic photovoltaic cells. Angew. Chem. Int. Ed. Engl. *59*, 9004–9010.

19. Classen, A., Chochos, C.L., Lüer, L., Gregoriou, V.G., Wortmann, J., Osvet, A., Forberich, K., McCulloch, I., Heumüller, T., and Brabec, C.J. (2020). The role of exciton lifetime for charge generation in organic solar cells at negligible energy-level offsets. Nat. Energy *5*, 711–719.

20. Ran, N.A., Roland, S., Love, J.A., Savikhin, V., Takacs, C.J., Fu, Y.T., Li, H., Coropceanu, V., Liu, X., Brédas, J.-L., et al. (2017). Impact of interfacial molecular orientation on radiative recombination and charge generation efficiency. Nat. Commun. *8*, 79.

21. Jain, N., Chandrasekaran, N., Sadhanala, A., Friend, R.H., McNeill, C.R., and Kabra, D. (2017). Interfacial disorder in efficient polymer solar cells: the impact of donor molecular structure and solvent additives. J. Mater. Chem. A *5*, 24749–24757.

22. Rosenthal, K.D., Hughes, M.P., Luginbuhl, B.R., Ran, N.A., Karki, A., Ko, S., Hu, H., Wang, M., Ade, H., and Nguyen, T. (2019). Quantifying and understanding voltage losses due to nonradiative recombination in bulk heterojunction organic solar cells with low energetic offsets. Adv. Energy Mater. *9*, 1901077.

23. Azzouzi, M., Yan, J., Kirchartz, T., Liu, K., Wang, J., Wu, H., and Nelson, J. (2018). Nonradiative energy losses in bulk-heterojunction organic photovoltaics. Phys. Rev. X *8*, 031055.

24. Li, T., Dai, S., Ke, Z., Yang, L., Wang, J., Yan, C., Ma, W., and Zhan, X. (2018). Fused Tris(thienothiophene)-based electron acceptor with strong near-infrared absorption for high-performance as-cast solar cells. Adv. Mater. *30*, 1705969.

25. Bixon, M., Jortner, J., and Verhoeven, J.W. (1994). Lifetimes for radiative charge recombination in donor-acceptor molecules. J. Am. Chem. Soc. *116*, 7349–7355.

26. Armin, A., Zarrabi, N., Sandberg, O.J., Kaiser, C., Zeiske, S., Li, W., and Meredith, P. (2020). Limitations of charge transfer state parameterization using photovoltaic external quantum efficiency. Adv. Energy Mater. *10*, 2001828.

27. List, M., Sarkar, T., Perkhun, P., Ackermann, J., Luo, C., and Würfel, U. (2018). Correct determination of charge transfer state energy from luminescence spectra in organic solar cells. Nat. Commun. *9*, 3631.

28. Vandewal, K., Gadisa, A., Oosterbaan, W.D., Bertho, S., Banishoeib, F., Van Severen, I., Lutsen, L., Cleij, T.J., Vanderzande, D., and Manca, J.V. (2008). The relation Between open-circuit voltage and the onset of photocurrent generation by charge-transfer absorption in polymer: fullerene bulk heterojunction solar cells. Adv. Funct. Mater. *18*, 2064–2070.

29. Zhang, M., Guo, X., Ma, W., Ade, H., and Hou, J. (2015). A large-bandgap conjugated polymer for versatile photovoltaic applications with high performance. Adv. Mater. *27*, 4655–4660.

30. Qian, D., Ye, L., Zhang, M., Liang, Y., Li, L., Huang, Y., Guo, X., Zhang, S., Tan, Z., and Hou, J. (2012). Design, application, and morphology study of a new photovoltaic polymer with strong aggregation in solution state. Macromolecules *45*, 9611–9617.

31. Lee, J., Ko, S.-J., Lee, H., Huang, J., Zhu, Z., Seifrid, M., Vollbrecht, J., Brus, V.V., Karki, A., Wang, H., et al. (2019). Side-chain engineering of nonfullerene acceptors for near-infrared organic photodetectors and photovoltaics. ACS Energy Lett *4*, 1401–1409.

32. Cowan, S.R., Roy, A., and Heeger, A.J. (2010). Recombination in polymer-fullerene bulk heterojunction solar cells. Phys. Rev. B *82*, 245207.

33. Sweetnam, S., Prasanna, R., Burke, T.M., Bartelt, J.A., and McGehee, M.D. (2016). How the energetic landscape in the mixed phase of organic bulk heterojunction solar cells evolves with fullerene content. J. Phys. Chem. C *120*, 6427–6434.

34. Sweetnam, S., Graham, K.R., Ngongang Ndjawa, G.O., Heumüller, T., Bartelt, J.A., Burke, T.M., Li, W., You, W., Amassian, A., and McGehee, M.D. (2014). Characterization of the polymer energy landscape in polymer:fullerene bulk heterojunctions with pure and mixed phases. J. Am. Chem. Soc. *136*, 14078–14088.

35. Xie, Y., Wang, W., Huang, W., Lin, F., Li, T., Liu, S., Zhan, X., Liang, Y., Gao, C., Wu, H., and Cao, Y. (2019). Assessing the energy offset at the electron donor/acceptor interface in organic solar cells through radiative efficiency measurements. Energy Environ. Sci. *12*, 3556–3566.

36. Karuthedath, S., Gorenflot, J., Firdaus, Y., Chaturvedi, N., De Castro, C.S.P., Harrison, G.T., Khan, J.I., Markina, A., Balawi, A.H., Peña, T.A.D., et al. (2021). Intrinsic efficiency limits in

low-bandgap nonfullerene acceptor organic solar cells. Nat. Mater. *20*, 378–384.

37. Perdigón-Toro, L., Phuong, L.Q., Zeiske, S., Vandewal, K., Armin, A., Shoaee, S., and Neher, D. (2021). Excitons dominate the emission from PM6:Y6 solar cells, but this does not help the open-circuit voltage of the device. ACS Energy Lett *6*, 557–564.

38. Xu, Y., Cui, Y., Yao, H., Zhang, T., Zhang, J., Ma, L., Wang, J., Wei, Z., and Hou, J. (2021). A new conjugated polymer that enables the integration of photovoltaic and light-emitting functions in one device. Adv. Mater. *33*, e2101090.

39. Jeon, S.O., Lee, K.H., Kim, J.S., Ihn, S.-G., Chung, Y.S., Kim, J.W., Lee, H., Kim, S., Choi, H., and Lee, J.Y. (2021). High-efficiency, long-lifetime deep-blue organic light-emitting diodes. Nat. Photonics *15*, 208–215.

40. Chan, C.-Y., Tanaka, M., Lee, Y.-T., Wong, Y.-W., Nakanotani, H., Hatakeyama, T., and Adachi, C. (2021). Stable pure-blue hyperfluorescence organic light-emitting diodes with high-efficiency and narrow emission. Nat. Photonics *15*, 203–207.

41. Wu, T.-L., Huang, M.-J., Lin, C.-C., Huang, P.-Y., Chou, T.-Y., Chen-Cheng, R.-W., Lin, H.-W., Liu, R.-S., and Cheng, C.-H. (2018). Diboron compound-based organic light-emitting

diodes with high efficiency and reduced efficiency roll-off. Nat. Photonics *12*, 235–240.

42. Kondo, Y., Yoshiura, K., Kitera, S., Nishi, H., Oda, S., Gotoh, H., Sasada, Y., Yanai, M., and Hatakeyama, T. (2019). Narrowband deep-blue organic light-emitting diode featuring an organoboron-based emitter. Nat. Photonics *13*, 678–682.

43. Ahn, D.H., Kim, S.W., Lee, H., Ko, I.J., Karthik, D., Lee, J.Y., and Kwon, J.H. (2019). Highly efficient blue thermally activated delayed fluorescence emitters based on symmetrical and rigid oxygen-bridged boron acceptors. Nat. Photonics *13*, 540–546.

44. Lee, Y.H., Park, S., Oh, J., Woo, S.-J., Kumar, A., Kim, J.-J., Jung, J., Yoo, S., and Lee, M.H. (2018). High-efficiency sky blue to ultradeep blue thermally activated delayed fluorescent diodes based on ortho -carbazole-appended triarylboron emitters: above 32% external quantum efficiency in blue devices. Advanced Optical Materials 6, 1800385.

45. Wei, Y.-C., Wang, S.F., Hu, Y., Liao, L.-S., Chen, D.-G., Chang, K.-H., Wang, C.-W., Liu, S.-H., Chan, W.-H., Liao, J.-L., et al. (2020). Overcoming the energy gap law in near-infrared OLEDs by exciton–vibration decoupling. Nat. Photonics *14*, 570–577.

46. Zampetti, A., Minotto, A., and Cacialli, F. (2019). Near-infrared (NIR) organic

light-emitting diodes (OLEDs): challenges and opportunities. Adv. Funct. Mater. *29*, 1807623.

47. Ullbrich, S., Benduhn, J., Jia, X., Nikolis, V.C., Tvingstedt, K., Piersimoni, F., Roland, S., Liu, Y., Wu, J., Fischer, A., et al. (2019). Emissive and charge-generating donor-acceptor interfaces for organic optoelectronics with low voltage losses. Nat. Mater. *18*, 459–464.

48. Chen, D., Xie, G., Cai, X., Liu, M., Cao, Y., and Su, S.J. (2016). Fluorescent organic planar pn heterojunction light-emitting diodes with simplified structure, extremely low driving voltage, and high efficiency. Adv. Mater. *28*, 239–244.

49. Beckers, O., Gielen, S., Verstraeten, F., Verstappen, P., Lutsen, L., Vandewal, K., and Maes, W. (2020). Continuous droplet flow synthesis of a near-infrared responsive push–pull copolymer toward large scale implementation of organic photodetectors. ACS Appl. Polym. Mater. *2*, 4373–4378.

50. Liu, Q., Gerling, L.G., Bernal-Texca, F., Toudert, J., Li, T., Zhan, X., and Martorell, J. (2020). Light harvesting at oblique incidence decoupled from transmission in organic solar cells exhibiting 9.8% efficiency and 50% visible light transparency. Adv. Energy Mater. *10*, 1904196.